^{99m}Tc sestamibi prone breast imaging for the diagnosis of breast carcinoma. *Radiology* 1995;196:421–426.
16. Khalkhali I, Cutrone J, Mena I, et al. Technetium-99m-sestamibi scintimammography of breast lesions: clinical and pathological follow-up. *J Nucl Med* 1995;36:1784–1789.
17. Palmedo H, Schomburg A, Grünwald F, Mallmann P, Krebs D, Biersack HJ. Technetium-99m-MIBI scintimammography for suspicious breast lesions. *J Nucl Med* 1996;37:626–630.
18. Taillefer R, Robidoux A, Lambert R, Turpin S, Laperriere J. Technetium-99m-sestamibi prone scintimammography to detect primary breast cancer and axillary lymph node involvement. *J Nucl Med* 1995;36:1758–1765.
19. Tiling R, Sommer H, Pechmann M, et al. Comparison of ^{99m}Tc sestamibi scintimammography with contrast-enhanced MRI for diagnosis of breast lesions. *J Nucl Med* 1997;38:58–62.
20. Waxman A, Nagaraj N, Ashok G, et al. Sensitivity and specificity of ^{99m}Tc methoxy isobutal isonitrile (MIBI) in the evaluation of primary carcinoma of the breast: comparison of palpable and nonpalpable lesions with mammography [Abstract]. *J Nucl Med* 1994;35:22.
21. Diggles L, Khalkhali I. SPECT prone dependent-breast scintimammography [Abstract]. *Eur J Nucl Med* 1994;21:769P.
22. Luig H, Eschner W, Bähre M, Voth E, Nolte G. An iterative strategy for determination of the source distribution in single-photon emission tomography with a rotating gamma camera (SPECT). *Nuklearmedizin* 1988;27:140–146.
23. Luig H, Eschner W, Nolte G, Bähre M, Voth E. In: Schmidt HAE, Csernay L, eds. *Multiplicative iterative SPECT reconstruction (MISR): an approach to exact absorption correction. New trends and possibilities in nuclear medicine.* Stuttgart, New York: Schattauer; 1988:101–104.
24. Kopans DB. The positive predictive value of mammography. *Am J Roentgenol* 1992;158:521–526.
25. Kopans DB. *Breast imaging.* Philadelphia: J.B. Lippincott Co., 1989:320.
26. Mena FJ, Mena I, Diggles LE, Khalkhali I. Design and assessment of a scintigraphy-guided biplane localization technique for breast tumours: a phantom study. *Nucl Med Commun* 1996;17:717–723.
27. Khalkhali I, Mishkin FS, Diggles LE, Klein SR. Radionuclide-guided localization of nonpalpable breast lesions in patients with normal mammograms. *J Nucl Med* 1997;38:1019–1022.

Quantitative Imaging of Iodine-131 Distributions in Brain Tumors with Pinhole SPECT: A Phantom Study

Mark F. Smith, David R. Gilland, R. Edward Coleman and Ronald J. Jaszczak
Departments of Radiology and Biomedical Engineering, Duke University Medical Center, Durham, North Carolina

A method of quantitatively imaging ^{131}I distributions in brain tumors from intratumoral administration of activity was developed and investigated using pinhole SPECT of brain tumor phantoms. **Methods:** Pinhole SPECT sensitivity and resolution were characterized using ^{131}I point-source acquisitions with high-resolution lead (1.4-mm diameter aperture) and tungsten (1.0-mm diameter aperture) pinhole inserts. SPECT scans were obtained from brain tumor phantoms in a water-filled cylinder. The tumor phantoms consisted of spheres filled with an ^{131}I solution to model intratumoral administration of radiolabeled monoclonal antibodies. Two spheres were 20.5 and 97 ml, and two other concentric spheres modeled a tumor with a high-activity shell (71.5 ml) and a low-activity core (21 ml). The collimator focal length was 16 cm and the distance from the pinhole to the center of rotation was 13 cm. The filtered backprojection reconstruction algorithm incorporated scatter and attenuation compensation. SPECT tumor activities and concentrations were estimated using scaling factors from reference point-source scans. **Results:** System sensitivities for point sources at the center of rotation were 28.4 cts/sec^{-1} MBq^{-1} (lead insert) and 13.6 cts/sec^{-1} MBq^{-1} (tungsten insert). SPECT resolutions (FWHM) at the center of rotation were 8.1–11.9 mm (lead) and 6.7–10.3 mm (tungsten). Total tumor activity estimates from SPECT were within 17% of the true activities. SPECT activity concentration estimates in small regions of interest (ROIs) averaged −20% for the 20.5-ml sphere, −11% for the 97-ml sphere, −39% for the shell and +20% for the core of the shell-core phantom. Activity spillover due to limited spatial resolution and the tails of the system response functions biased the estimates. The shell-to-core activity concentration ratio of 4.1 was better estimated with the tungsten insert (2.3) than with the lead insert (1.9) due to better resolution. **Conclusion:** Pinhole SPECT is a promising technique for imaging and quantifying total ^{131}I activity in regions the size of brain tumors. Relative errors were greater for activity concentration estimates in small ROIs than for total activity estimates.

Key Words: pinhole collimator; SPECT; iodine-131 imaging; brain tumor; radioimmunotherapy

J Nucl Med 1998; 39:856–864

The administration of ^{131}I-labeled monoclonal antibodies is a promising strategy for the treatment of malignant tumors (*1,2*). With intratumoral administration of activity, antibody uptake in the tumor is markedly increased relative to intravenous administration (*3,4*). High resolution SPECT imaging will allow the time-dependent three-dimensional accumulation of ^{131}I radiolabeled antibody in the tumors to be followed and will permit better evaluation of tumor dosimetry (*5*). In Phase I studies of ^{131}I radioimmunotherapy at Duke University Medical Center, Durham, NC (*6,7*), 1850–3700 MBq (50–100 mCi) ^{131}I have been administered directly into cystic brain tumors or postoperative resection cavities and intrathecally. We are investigating clinically practical

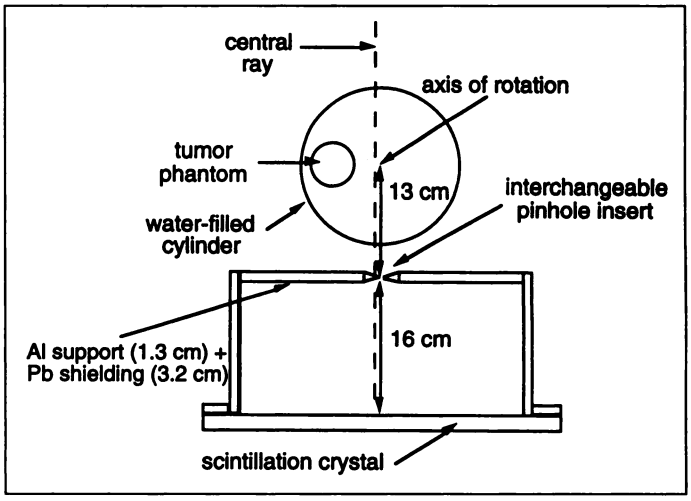

FIGURE 1. Diagram of the pinhole apparatus mounted on one head of a Trionix Triad gamma camera. Also shown is the position of the water-filled cylinder for the SPECT acquisitions and an off-center tumor phantom position.

Received Feb. 1, 1997; revision accepted Jul. 4, 1997.
For correspondence or reprints contact: Mark F. Smith, PhD, National Institutes of Health, Nuclear Medicine Department, Bldg. 10, Rm. 1C401, 10 Center Dr., MSC 1180, Bethesda, MD 20892.

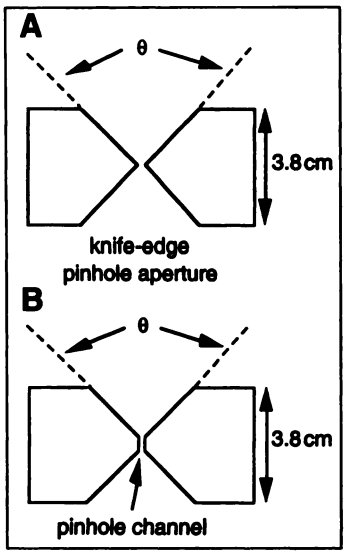

FIGURE 2. Design of the pinhole inserts. The acceptance angle θ is indicated. (A) Knife-edge aperture design for the lead insert and (B) channel aperture design for the tungsten insert.

ways to use SPECT to image and quantify antibody uptake within these tumors to aid tumor dosimetry calculations and the assessment of the clinical effectiveness of radioimmunotherapy.

The gamma-ray emissions that accompany the beta-particle emission by ^{131}I allow the distribution of ^{131}I to be imaged by gamma cameras. The primary gamma-ray emission is at 364 keV (82% abundant), with additional emissions at 637 keV (6.5%) and 723 keV (1.7%) (*8*). High-resolution, quantitative SPECT is more difficult with ^{131}I than with lower energy radionuclides because of the increased penetration of these medium- and high-energy emissions. Pinhole SPECT is one approach to limit penetration and to achieve high resolution with acceptable sensitivity (*9,10*).

We have previously shown that pinhole SPECT is a viable technique for imaging the medium-energy 171- and 245-keV emissions of ^{111}In in head phantoms (*11*), and that pinhole imaging can provide improved performance over parallel-hole collimators for imaging ^{131}I in a head phantom (*12*). Gamma camera imaging of ^{131}I with parallel-hole collimators also has been investigated recently by other research groups (*13–18*).

In this study, we developed and investigated a method to quantitatively image the distribution of ^{131}I in brain tumors using pinhole SPECT of brain tumor phantoms. The sensitivity and resolution of our pinhole SPECT imaging system with high-resolution pinhole apertures are characterized. A scaling procedure for converting counts in reconstructed ^{131}I SPECT scans to absolute activities is described. SPECT scans of various brain tumor phantoms in a water-filled cylinder are obtained. The total activity and radionuclide concentrations in the brain tumor phantoms are estimated from the SPECT scans and are compared with the true activities and concentrations.

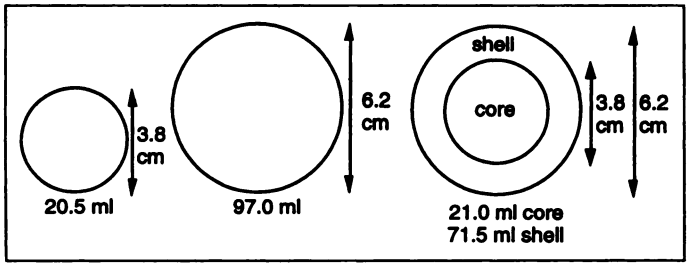

FIGURE 3. Diagram of the tumor phantoms that were filled with ^{131}I solution, with outer diameters indicated. The plastic used to fabricate the phantoms was about 1.5 mm thick.

TABLE 1
System Sensitivity for a Point Source 13 cm Above the Pinhole at the Center of Rotation

Insert type	Sensitivity (counts sec^{-1} MBq^{-1}) Counting threshold: None (all counts included)	Sensitivity (counts sec^{-1} MBq^{-1}) Counting threshold: 10% of maximum pixel value
Lead	28.4	15.4
Tungsten	13.6	5.70

MATERIALS AND METHODS

Pinhole SPECT Apparatus

Planar and SPECT scans were acquired on a Triad gamma camera (Trionix Research Laboratory, Twinsburg, OH) using a custom-built pinhole imaging apparatus (Fig. 1). The apparatus was box-shaped with an aluminum support structure and lead shielding. The focal length (pinhole to scintillation crystal distance) was 16 cm. The pinhole insert was interchangeable and two different pinhole inserts were used for the gamma camera acquisitions. The aperture of the lead insert was 1.42 ± 0.05 mm diameter with an acceptance angle of 100° and a knife-edge taper (Fig. 2A). The aperture of the tungsten insert was 0.96 ± 0.03 mm diameter with an acceptance angle of 100° and a 1.5-mm high channel designed to reduce penetration near the aperture (Fig. 2B). These high-resolution apertures were smaller than the 3–6 mm diameter apertures used in our previous head imaging experiments (*11,12*). Considerations in the design of channeled pinhole apertures for ^{131}I imaging have been previously discussed (*19*).

System Sensitivity and Resolution

The system sensitivity and resolution were measured using point-source scans with the lead and tungsten inserts. The point source contained 10.0 MBq (0.271 mCi) ^{131}I. Planar scans were 5 min duration and SPECT scans were 20 min duration, with projection data acquired for 10 sec/angle at 120 equally spaced angles over 360°. The energy windows were 364 keV ± 9% (photopeak) and 304 keV ± 9% (scatter). The projection pixels were 1.78 mm on a side. Planar scans were acquired with the point source in air 13 cm above the pinhole on the central ray. The system sensitivities were calculated in two ways: first by summing the total number of counts in the projection data and second by summing counts above 10% of the maximum pixel value. The latter estimate excluded counts due to scatter and penetration near the pinhole aperture that contributed to the tails of the point-source response functions and degraded system resolution.

SPECT scans were acquired with the point source in air and in water, both at the center of rotation and 6.2 cm off-center. The pinhole aperture was 13 cm from the center of rotation. For the scans in water, the axis of the 23-cm diameter water-filled cylinder was aligned with the axis of rotation of the gamma camera (Fig. 1). The projection data array was 256 × 128 with 1.78 mm pixels. A $\cos^x(\theta)$ offset-dependent sensitivity correction (*20*) was applied to the projection data using $x = 6.4$ (lead insert) and $x = 8.5$ (tungsten insert) determined from point-source sensitivity measurements. Scatter compensation for the scans in water was accomplished by

TABLE 2
Planar System Resolution for a Point Source 13 cm Above the Pinhole at the Center of Rotation

Insert type	FWHM (mm)	FWTM (mm)
Lead	9.0	22.5
Tungsten	7.4	17.2

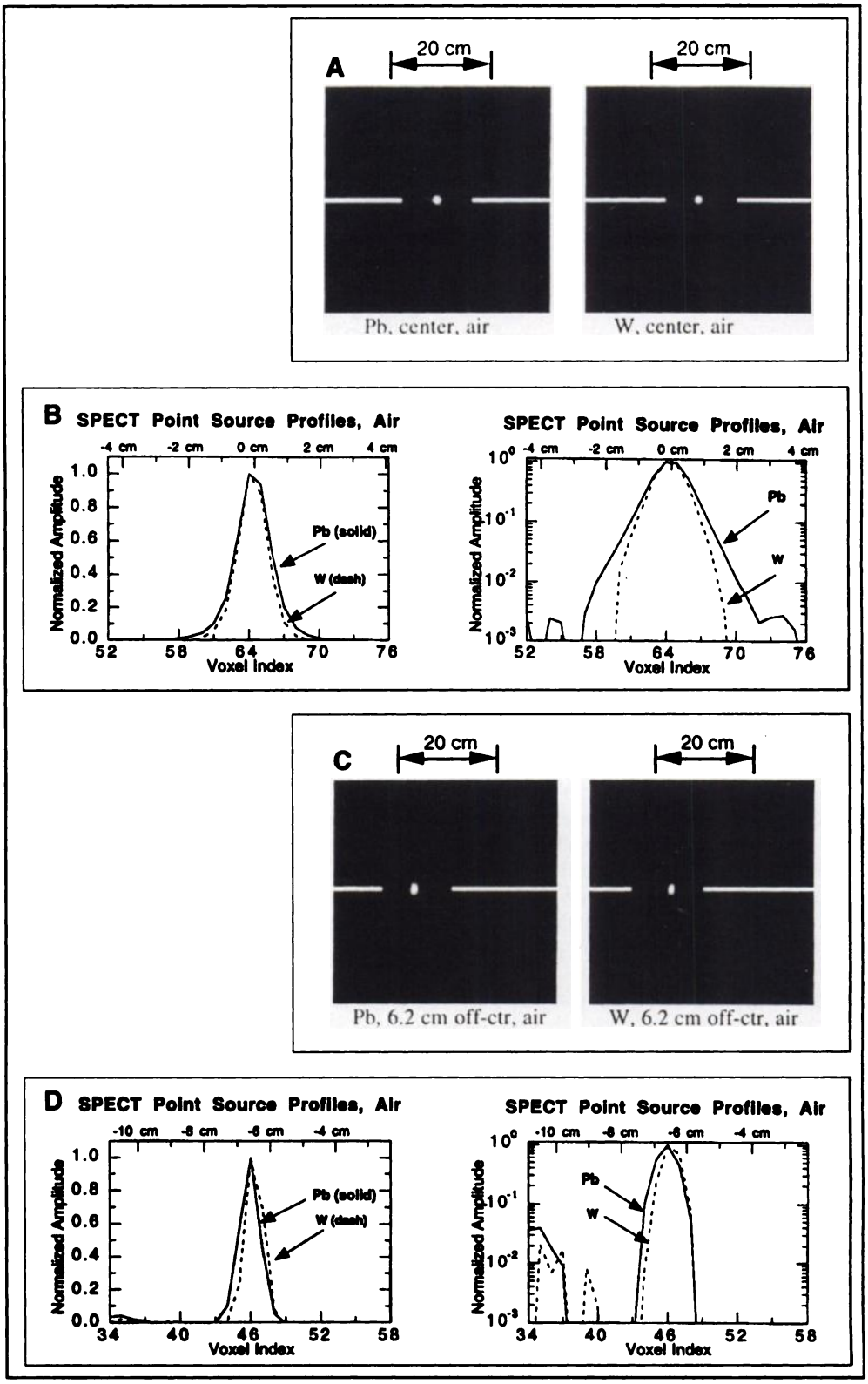

FIGURE 4. SPECT reconstructions (Hann filter cutoff 1.40 cycles/cm) and profiles for point sources in air acquired with the lead and tungsten pinhole inserts. (A) Point source at the center of rotation, (B) profiles from Figure 4A, (C) point source 6.2 cm off-center and (D) profiles from Figure 4C. The profiles are normalized to their maximum voxel value. The tails are due in part to penetration through and scatter within the pinhole insert. Some reconstruction edge artifacts are seen for the 6.2 cm off-center location.

scatter subtraction (*21*) using a *k*-factor of 1.0. This *k*-factor was determined using the point-source measurements in air and in water for the photopeak and scatter energy windows used in this study. The chosen *k*-factor provided compensation for scattered photons observed in the photopeak energy window.

Pinhole SPECT reconstruction was accomplished using a filtered backprojection approach (*22*). The reconstructed voxel size was 1.78 mm. Reconstructions with a ramp filter were too noisy to allow reliable assessment of system resolution, so reconstructions were performed with two-dimensional Hann filters applied to the projection data. The high frequency cutoffs of these filters were Nyquist (2.81 cycles/cm) and half-Nyquist (1.40 cycles/cm) frequencies in projection space (the lower cutoff was the one applied later to the brain tumor phantom reconstructions to suppress high-frequency noise). A multiplicative Chang attenuation correction (*23*) was applied for the scans in water. The attenuation map was constructed using the physical dimensions of the cylinder and the attenuation coefficient of water at 364 keV.

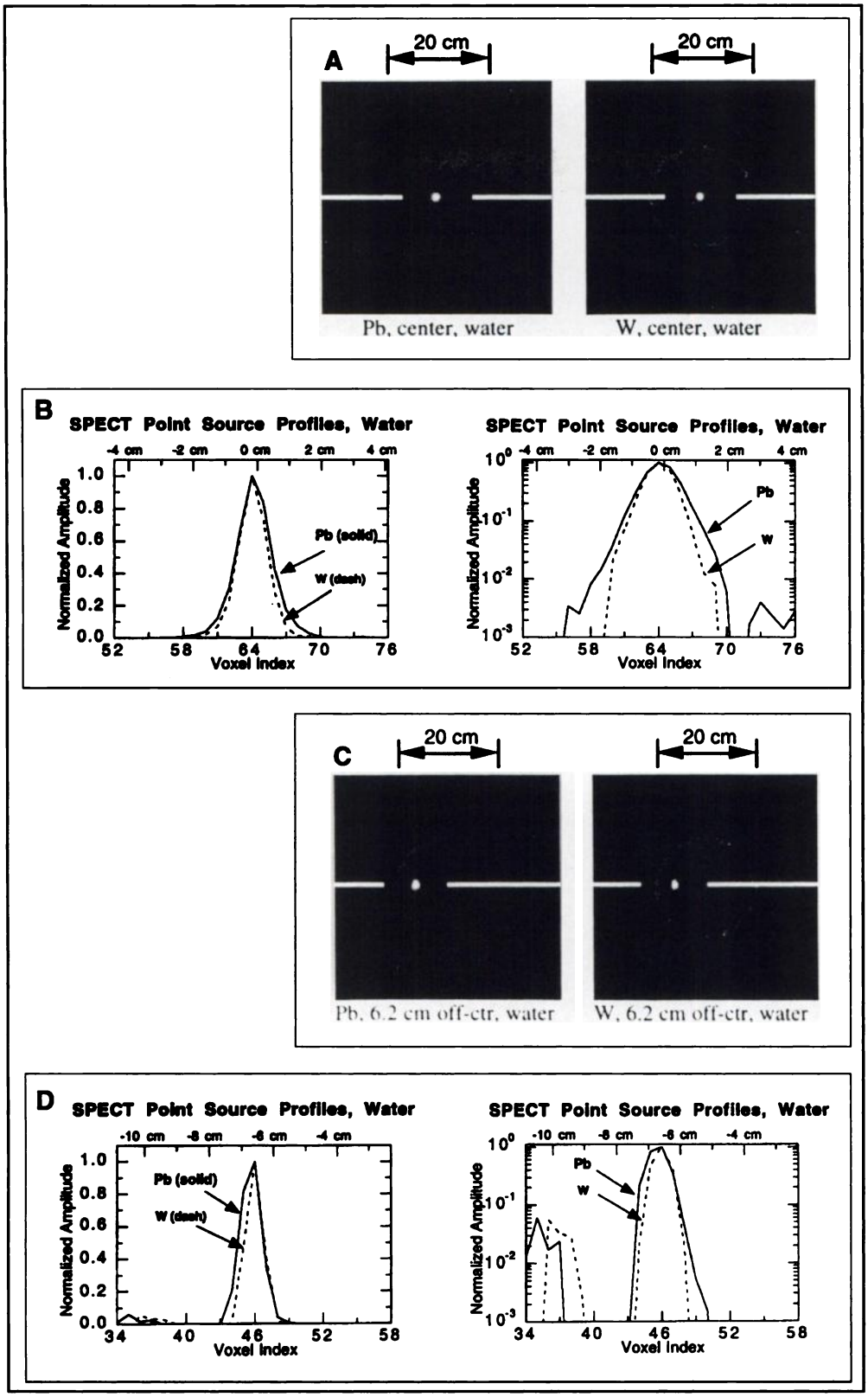

FIGURE 5. SPECT reconstructions (Hann filter cutoff 1.40 cycles/cm) and profiles for point sources in water acquired with the lead and tungsten pinhole inserts. (A) Point source at the center of rotation, (B) profiles from Figure 5A, (C) point source 6.2 cm off-center and (D) profiles from Figure 5C. The profiles are normalized to their maximum voxel value. The tails are due in part to penetration through and scatter within the pinhole insert, as well as to scatter in the water-filled cylinder. Some reconstruction edge artifacts are seen for the 6.2 cm off-center location.

Scaling Factors for SPECT Quantitation

Scaling factors obtained with the reference point source were used to convert counts in the reconstructed SPECT scans to measured activities:

$$\text{SPECT activity (MBq)} = \text{SPECT image counts} \times \text{scaling factor (MBq/count)}. \quad \text{Eq. 1}$$

Scaling factors were determined using the reconstructed SPECT scan of the reference point-source in air at the center of rotation. First, the maximum voxel value in the reconstructed point source image was found. Then, a family of scaling factors was generated by considering voxels with counts above given percentages of the maximum voxel value that were connected to the peak voxel value by other voxels that were also above the given threshold. The scaling factor was given by:

TABLE 3
SPECT System Resolution from Point-Source Scans (Hann Filter Cutoff Frequency Indicated)

Scan medium	Source location	Profile direction	FWHM (mm)				FWTM (mm)			
			Lead		Tungsten		Lead		Tungsten	
			2.81 cycles/cm	1.40 cycles/cm	2.81 cycles/cm	1.40 cycles/cm	2.81 cycles/cm	1.40 cycles/cm	2.81 cycles/cm	1.40 cycles/cm
Air	At COR	Radial	8.1	11.8	6.7	10.3	18.4	24.4	16.2	20.3
Water	At COR	Radial	8.5	11.9	7.2	10.3	19.2	24.8	15.9	20.6
Air	6.2 cm off-center	Radial	6.1	7.3	5.3	7.0	11.1	13.8	10.4	12.6
Air	6.2 cm off-center	Tangential	8.2	10.1	6.5	9.3	22.1	23.8	15.6	20.5
Water	6.2 cm off-center	Radial	6.4	8.1	6.0	6.3	11.0	15.3	9.5	12.8
Water	6.2 cm off-center	Tangential	7.6	9.5	6.2	7.9	20.1	20.3	17.7	16.9

Estimated errors: ± 0.4 mm FWHM, ± 0.6 mm FWTM. COR = center of rotation.

Scaling factor = reference point-source activity from well counter (MBq)/SPECT counts for reference point source above a calibration threshold. Eq. 2

It is not obvious a priori what percentage threshold should be used for accurate SPECT activity quantitation with brain tumors, since the tails from point-source response functions will add constructively in the center of larger source regions. We took the approach of determining the appropriate calibration thresholds empirically, as will be discussed in the Results section of this article. The SPECT images of the point sources used to determine the scaling factors were reconstructed with the same filter used to reconstruct the tumor phantom images.

SPECT Scans of Brain Tumor Phantoms

Acquisition. SPECT scans were obtained of three brain tumor phantoms placed in the water-filled cylinder modeling the head. The phantoms consisted of two hollow spheres, 20.5 and 97.0 ml, and one set of two other concentric spheres (Fig. 3). For the latter phantom, the outer shell region was 71.5 ml and the inner core region was 21.0 ml. This shell-core tumor phantom modeled the case of a tumor with regions of different radiopharmaceutical uptake, as might be the case for an actively growing tumor with malignant cells at the periphery and a necrotic core.

Iodine-131 activity was drawn up in a syringe and assayed in a dose calibrator before dilution with water of measured volumes and injection into the tumor phantoms. The 20.5-ml sphere was filled with an aqueous solution of 33.0 MBq ^{131}I for a concentration of 1.61 MBq/ml. The 97.0-ml sphere was filled with 182 MBq or 1.88 MBq/ml. The shell-core phantom was filled with ^{131}I solutions of different concentrations. The shell was filled with 115 MBq for a concentration of 1.61 MBq/ml, and the core was filled with 8.27 MBq for a concentration of 0.394 MBq/ml. The shell-to-core activity concentration ratio was 4.09.

The tumor phantoms were imaged individually without background activity with both the lead and tungsten pinhole inserts. Separate SPECT scans were acquired with the centers of the phantoms 1.1 cm and 6.2 cm from the axis of the water-filled cylinder. The scans were 60 min, with projection data acquired at 120 equally spaced angles over 360°. The energy windows were 364 keV ± 9% (photopeak) and 304 keV ± 9% (scatter). The projection array was 256 × 128 and the 1.78 mm projection pixels were summed to 3.56 mm pixels for image reconstruction.

Reconstruction. The projection data were reconstructed in a fashion similar to that for the point-source scans in water. In particular, an offset-dependent sensitivity correction was applied and a scatter subtraction factor $k=1.0$ was used for dual-energy window scatter compensation. A two-dimensional Hann filter with a high frequency cutoff of 1.40 cycles/cm in projection space was applied to the projection data to suppress high-frequency noise in the reconstructed images. A one-iteration Chang attenuation correction was applied.

Activity Quantitation. The total tumor activity and radionuclide concentrations in small regions of interest (ROIs) in the tumor phantoms were estimated using the SPECT reconstructions. Total SPECT tumor activities were estimated using the following procedure:

1. The average voxel value in a small ROI in a region of the image with peak activity was computed. The ROI was drawn manually and was 6 × 6 voxels for the 97-ml tumor, 4 × 4 voxels for the 20.5 ml-tumor and 8 × 3 voxels for the shell region of the shell-core phantom.
2. A loose three-dimensional spherical ROI was centered around the tumor. This was accomplished by manually adjusting the center and radius of a digital mask that zeroed activity outside of the ROI. The ROI diameter was 10 cm for the 97-ml and shell-core tumors located 1.1 cm off-center and 9 cm for these tumors 6.2 cm off-center. The ROI diameter was 7 cm for the 20.5-ml tumor located 1.1 cm off-center and 5 cm for the 6.2-cm off-center location. The resulting masked images were visually inspected to verify that the ROIs were properly chosen. Counts from voxels within the loose ROI with amplitudes greater than 10% of the peak activity average of Step 1 were summed. This 10% threshold was chosen to allow summing of as many of the reconstructed tumor counts as possible and still remain above the background noise level.
3. The summed counts were converted to absolute activities using scaling factors from the reference point sources. Activity estimates were calculated for different calibration thresholds (see Eqs. 1 and 2 and the point-source experiments described in the earlier section on scaling factors).

Tumor radionuclide concentrations were estimated using small ROIs within the reconstructed images in the regions of peak activity as described in Step 1. A 27-voxel ROI also was selected in the center of the core of the shell-core phantom. The ROIs were drawn manually and were chosen as large as possible (to reduce statistical noise) within regions of approximately constant activity. Using the volume of the ROI and the number of counts in the ROI, the radionuclide concentration (MBq/ml) was computed for a range of calibration thresholds.

RESULTS

System Sensitivity and Resolution

Sensitivity and resolution for acquisition geometries appropriate for brain imaging were measured. Sensitivities with the

TABLE 4
Projection Data Counts in the Tumor Phantom Studies

Phantom	Insert type	Phantom location	Counts (× 10^6)
20.5-ml sphere	Pb	1.1 cm off-center	1.5
	Pb	6.2 cm off-center	1.8
	W	1.1 cm off-center	0.70
	W	6.2 cm off-center	0.82
97-ml sphere	Pb	1.1 cm off-center	7.5
	Pb	6.2 cm off-center	9.4
	W	1.1 cm off-center	3.4
	W	6.2 cm off-center	4.1
Shell-core	Pb	1.1 cm off-center	5.7
	Pb	6.2 cm off-center	7.0
	W	1.1 cm off-center	2.6
	W	6.2 cm off-center	3.0

Pb = lead; W = tungsten.

point source 13 cm above the pinhole at the center of rotation are given in Table 1. The sensitivities were smaller when an amplitude threshold of 10% of the maximum pixel value was used, illustrating the large fraction of scattered and penetrating photons. The planar system resolution for a point source at the center of rotation (corrected for magnification) is given in Table 2. The improved resolution with the tungsten insert was due to both the narrower pinhole diameter and the additional attenuation of the channeled aperture.

SPECT reconstructions and profiles with the point source at the center of rotation (13 cm above the pinhole aperture on the central ray) and 6.2 cm off-center are shown in Figures 4 and 5. The width of the system response function was narrower with the tungsten pinhole insert than with the lead insert. SPECT resolutions for the different pinhole collimators and reconstruction filters are given in Table 3. The radial resolution is the resolution along the line connecting the point source with the center of rotation (horizontal profile in Figs. 4 and 5) and the tangential resolution is the resolution along the line passing through the point source perpendicular to this radial line. Resolution was about the same in air and in water. Radial resolution was better than tangential resolution, and resolution was better at the edge of the field of view than at the center of rotation. The SPECT resolutions with the lead (tungsten) insert were 6–9 (5–7) mm FWHM for a Hann filter cutoff of 2.81 cycles/cm and 7–12 (6–10) mm FWHM for a cutoff of 1.40 cycles/cm.

Brain Tumor Phantom Studies

The brain tumor phantom studies contained between 700,000 and 9.4 million counts (Table 4). More counts were obtained at the 6.2 cm off-center position because of greater geometric sensitivity (inversely proportional to distance squared) and less attenuation when the tumor phantoms were closer to the pinhole. Reconstructed slices and profiles (Fig. 6) show that resolution and contrast were improved with the narrower tungsten pinhole insert, though at the expense of increased image noise due to lower sensitivity. The shell of the shell-core phantom was higher in intensity toward the periphery of the cylinder because image resolution was spatially varied and better toward the outside, resulting in higher reconstructed voxel amplitudes.

Results from estimation of total activity in the brain tumor phantoms are shown in Figure 7. The activity estimates increased as the calibration threshold used in the calculation of the scaling factor from the reference point-source data increased. An appropriate average value of the calibration threshold was about 17% with the lead pinhole insert and 11% with the tungsten insert. The total tumor activities and errors in these activities were estimated using these empirically-determined thresholds (Table 5). The total tumor activities were accurate to within 17%.

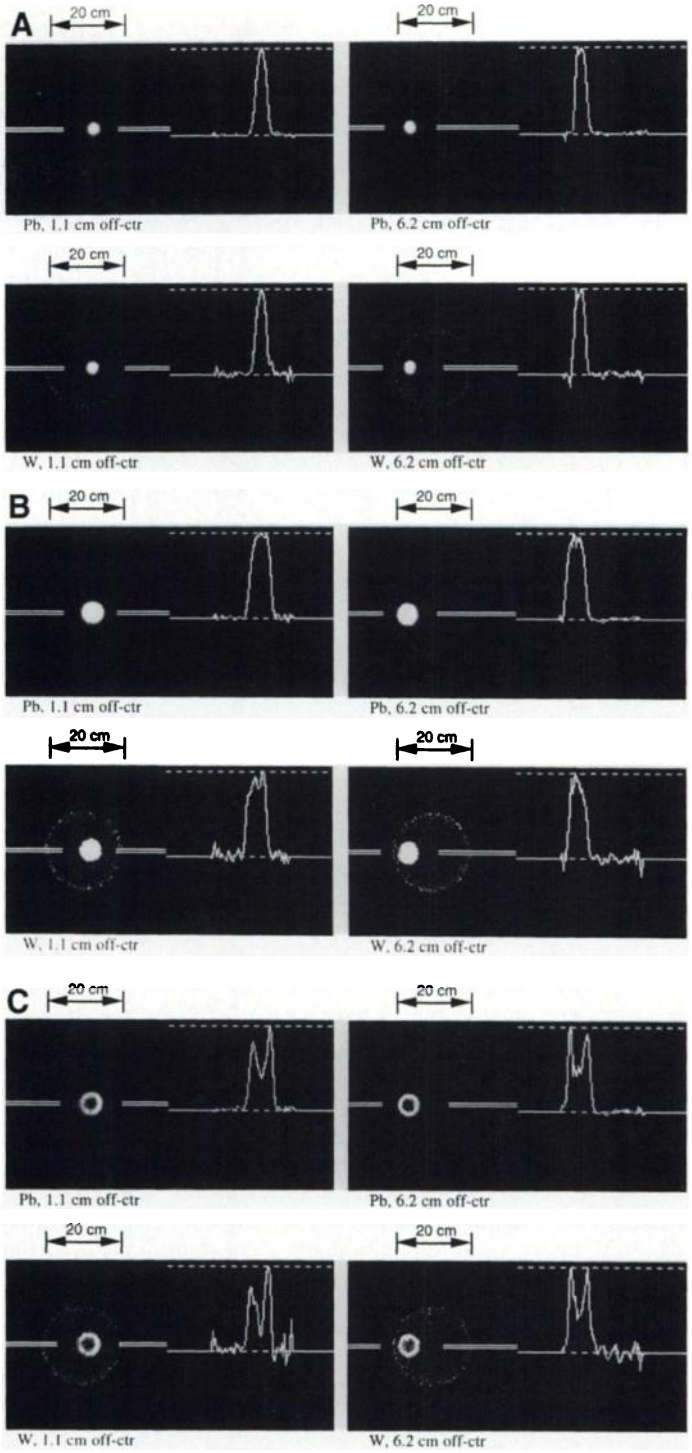

FIGURE 6. Reconstructed images and profiles from the tumor phantom studies. These transverse slices pass through the center of the tumors. (A) 20.5-ml tumor phantom, (B) 97-ml tumor phantom and (C) shell-core tumor phantom.

The radionuclide concentrations in the small ROIs varied as a function of calibration threshold (Fig. 8). As previously mentioned, finite spatial resolution and the tails of the system response functions caused activity spillover into low-activity

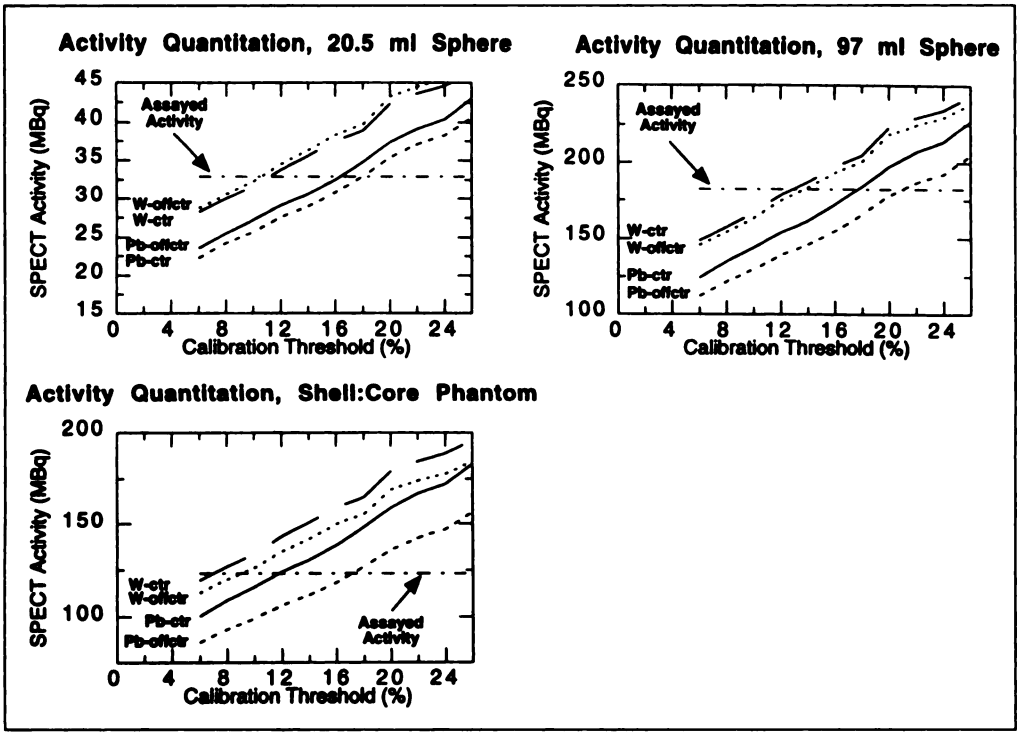

FIGURE 7. Total activity quantitation for the different tumor phantoms. The calibration threshold for the scaling factor was varied. Lead collimator, near-center position (solid); lead collimator, 6.2 cm off-center position (medium dash); tungsten collimator, near-center position (long dash); tungsten collimator, 6.2 cm off-center position (short dash); assayed activity from well counter (dotted dash).

regions. The high-activity regions were also different sizes and shapes, so it was not possible to choose one set of calibration thresholds that would result in accurate activity estimates in all of the ROIs. Thus, we used the 17% and 11% calibration thresholds for the lead and tungsten inserts derived from the total tumor activity estimates and provide the resulting radionuclide concentration estimates using these thresholds in Table 6.

Activity concentrations in the center of the tumor phantoms were underestimated by an average of 20% for the 20.5-ml tumor. This was larger than the average underestimate of 11% for the 97-ml tumor. For the shell-core phantom, the activity concentration in the low-activity core was overestimated by an average of 20% due to spillover from the higher activity shell. The activity concentration in the shell was underestimated by an average of 39% due to activity spillover into the core and outside of the tumor. Shell-to-core activity concentration ratios were calculated using the radionuclide concentrations in Table 6. For this experiment, the true value of the activity concentration ratio was 4.1; SPECT estimates of these ratios averaged 1.9 with the lead insert and 2.3 with the tungsten insert. The value with the tungsten insert was more accurate due to better resolution.

DISCUSSION

The SPECT quantitation method described in this article can be compared with other reported methods for ^{131}I quantitation. Israel et al. (*13*) acquired SPECT data for 25- to 127-cc spheres in an Alderson body phantom and used a thresholding technique to estimate tumor volumes. They found that a threshold that was 43% of the maximum voxel value provided volume estimates that best matched the phantom volumes. An empirically determined scaling factor was used to convert SPECT counts/voxel into activity concentration (μCi/cc). Green et al. (*14*) investigated the case of ^{131}I sources in a torso phantom and compensated for scatter by using a secondary energy window subtraction technique originally proposed by Jaszczak for ^{99m}Tc (*21*). An empirically determined scaling factor was used to convert SPECT counts/voxel to activity concentration (μCi/ml). Gilland et al. (*12*) used a point-source calibration procedure for ^{131}I

TABLE 5
Total Activity Quantitation (Calibration Thresholds 17% for Lead Insert, 11% for Tungsten Insert)

Phantom	Pinhole insert	Phantom location	SPECT activity (MBq)	Error (%)
20.5-ml sphere	Pb	1.1 cm off-center	33.8	+2.4
	Pb	6.2 cm off-center	32.0	−3.0
	W	1.1 cm off-center	32.7	−0.9
	W	6.2 cm off-center	33.4	+1.2
97-ml sphere	Pb	1.1 cm off-center	179	−1.6
	Pb	6.2 cm off-center	161	−11.5
	W	1.1 cm off-center	172	−5.5
	W	6.2 cm off-center	169	−7.1
Shell-core	Pb	1.1 cm off-center	144	+16.8
	Pb	6.2 cm off-center	123	−0.2
	W	1.1 cm off-center	139	+12.8
	W	6.2 cm off-center	131	+6.3

Pb = lead; W = tungsten.

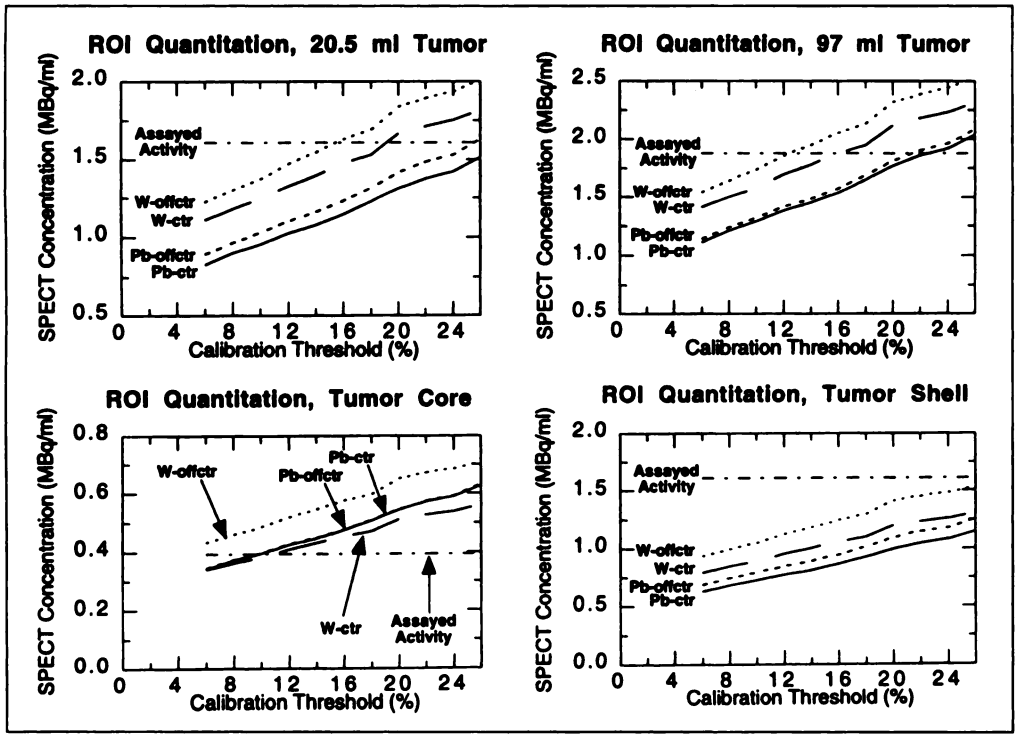

FIGURE 8. Activity concentrations for the 20.5- and 97-ml tumor phantoms from small ROIs near the center of the tumors, and for the shell-core phantom from small ROIs within the shell and core. Lead collimator, near-center position (solid); lead collimator, 6.2 cm off-center position (medium dash); tungsten collimator, near-center position (long dash); tungsten collimator, 6.2 cm off-center position (short dash); assayed activity from well counter (dotted dash).

source vials in a head phantom. A fixed threshold of 10% of the maximum voxel value was used for the SPECT reconstruction of a point source using a Hann filter. The voxel threshold for sources in the head phantom was varied to find the value that provided the most accurate activity (mCi) estimates. The best threshold was approximately 10% when a Hann filter was used for reconstruction and 20% when a Metz filter was used. Together with the calibration technique and results reported in this article, these studies indicate that acceptable ^{131}I SPECT activity estimates can be obtained with careful attention to calibration for the specific quantitation task.

Accurate activity quantitation for ^{131}I SPECT imaging is dependent on many factors, not all of which have been examined in this study. The scaling factors to convert SPECT counts into absolute activities depend in part on the SPECT gamma camera, acquisition parameters and the image reconstruction method. We are currently studying ways to model the tails of ^{131}I system response functions due to penetration near the pinhole aperture to implement resolution recovery filters (*24*).

The quantitation method presented here was designed for the task of estimating tumor activity for intratumoral administration of ^{131}I radiolabeled monoclonal antibodies, where counts in the projection data are expected to be high, the background activity is expected to be very low and tumor-to-background contrast is expected to be high. Quantitation in small regions of tumors with heterogeneous radionuclide uptake is difficult even with high-resolution SPECT, and larger relative errors are expected as the volume of the ROI decreases. With fewer counts in the projection data, regional activity estimates will be less accurate due to statistical noise in the projection data; additional filtering

TABLE 6
Tumor Radionuclide Concentration Using Small ROIs (Calibration Thresholds 17% for Lead Insert, 11% for Tungsten Insert)

Phantom/ROI location	Pinhole insert	Phantom location	SPECT Concentration (MBq/ml)	Error (%)
20.5-ml sphere	Pb	1.1 cm off-center	1.19	−26.1
	Pb	6.2 cm off-center	1.28	−20.5
	W	1.1 cm off-center	1.29	−19.9
	W	6.2 cm off-center	1.42	−11.8
97-ml sphere	Pb	1.1 cm off-center	1.60	−14.9
	Pb	6.2 cm off-center	1.64	−12.8
	W	1.1 cm off-center	1.64	−12.7
	W	6.2 cm off-center	1.79	−4.8
Core of shell-core	Pb	1.1 cm off-center	0.493	+25.1
	Pb	6.2 cm off-center	0.495	+25.6
	W	1.1 cm off-center	0.396	+0.5
	W	6.2 cm off-center	0.503	+27.7
Shell of shell-core	Pb	1.1 cm off-center	0.901	−44.0
	Pb	6.2 cm off-center	0.984	−38.9
	W	1.1 cm off-center	0.925	−42.5
	W	6.2 cm off-center	1.09	−32.3

Pb = lead; W = tungsten.

to reduce image noise will bias these estimates by blurring the reconstructed image. Determining the quantitative accuracy of tumor activity estimates for different tumor sizes and shapes, different wall thicknesses and different activity concentrations within the tumor and background regions is an area for future research.

One of our goals is to develop a patient-independent technique for ^{131}I SPECT quantitation. The quantitation method proposed in this article will be particularly valuable when a reference patient scan cannot be obtained immediately postinjection, or when the tracer is introduced gradually into the tumor rather than being administered as a bolus injection. The results of this study show that no single scaling factor can be applied to SPECT reconstructions of different source activity distributions and result in accurate tumor activity estimates. This implies that one must be cautious in applying a single scaling factor, as the biodistribution of the radiolabeled monoclonal antibody inside the tumor changes with time.

In this article we considered a tumor model within a uniformly attenuating water-filled cylinder. The most accurate clinical SPECT quantitation will require compensation for nonuniform attenuation within the head and skull. Kemp et al. (*25*) have found that good SPECT uniformity for a ^{99m}Tc (140-keV photopeak) brain tracer was obtained with an attenuation correction method that modeled different attenuation within the soft tissue and bone. Turkington et al. (*26*) reported that skull attenuation for ^{99m}Tc resulted in relative attenuation increases of less than 6%. Stodilka et al. (*27*) have found that relative quantitation within 10% can be achieved for ^{99m}Tc using a contour of the head boundary and a uniform Chang attenuation correction, but that more accurate quantitation required nonuniform attenuation correction. In a study with ^{123}I (159-keV photopeak) Rajeevan et al. (*28*) reported quantitative errors of 12% in the midbrain and 5% in the striatum when uniform rather than nonuniform attenuation correction methods were used. Nonuniform attenuation correction for ^{131}I imaging of the head has yet to be investigated.

CONCLUSION

Our measurements demonstrate that high resolution and good sensitivity for ^{131}I SPECT imaging can be achieved with a pinhole collimator apparatus mounted on a clinical gamma camera and using high-resolution pinhole apertures. SPECT scans of three brain tumor phantoms from 20–100 ml modeling intratumoral administration of activity show that total tumor activities can be measured within 17% with a method of scaling the SPECT image counts using a reference point-source scan. The use of appropriate scaling factors is especially important for ^{131}I imaging due to penetration and scatter near the pinhole aperture. Relative quantitation errors are greater for radionuclide concentration estimation in small ROIs. Shell-to-core radionuclide concentration ratios in the shell-core tumor phantom are more accurate with a tungsten pinhole insert than with a lead insert due to better resolution. Pinhole SPECT is a promising technique for imaging and quantifying ^{131}I activity in regions the size of brain tumors. Further investigation is needed with phantoms that more accurately model the nonuniform attenuation properties of the human head. Application of the quantitation techniques described in this article to patients who are being treated with direct administration of ^{131}I-monoclonal antibodies into brain tumors is planned.

ACKNOWLEDGMENTS

This work was supported by grant DE-FG02–96ER62150 from the U.S. Department of Energy and PHS grants R01-CA33541 and R29-HL52162 from the National Institutes of Health, Bethesda, MD. We thank Capt. William Briner, John Herman, RPh Tech. and Kim Greer, CNMT for support of and assistance with the experimental data acquisition. The shell-core tumor phantom was loaned by Data Spectrum Corp., Hillsborough, NC.

REFERENCES

1. Larson SM. Radiolabeled monoclonal anti-tumor antibodies in diagnosis and therapy. *J Nucl Med* 1985;26:538–545.
2. Goldenberg DM, Blumenthal RD, Sharkey RM. Biological and clinical perspectives of cancer imaging and therapy with radiolabeled antibodies. *Semin Cancer Biol* 1990;1: 217–225.
3. Epenetos AA, Munro AJ, Stewart S, et al. Antibody-guided irradiation of advanced ovarian cancer with intraperitoneally administered radiolabeled monoclonal antibodies. *J Clin Oncol* 1987;5:1890–1899.
4. Riva P, Arista A, Tison V, et al. Intralesional radioimmunotherapy of malignant gliomas. *Cancer* 1994;73:1076–1082.
5. Leichner PK, Koral KF, Jaszczak RJ, Green AJ, Chen GTY, Roeske JC. An overview of imaging techniques and physical aspects of treatment planning in radioimmunotherapy. *Med Phys* 1993;20:569–577.
6. Bigner DD, Brown M, Coleman RE, et al. Phase I studies of treatment of malignant gliomas and neoplastic meningitis with ^{131}I-radiolabeled monoclonal antibodies anti-tenascin 81C6 and anti-chondroitin proteoglycan sulfate Mel–14 F $(ab')_2$: a preliminary report. *J Neurooncol* 1995;24:109–122.
7. Brown MT, Coleman RE, Friedman AH, et al. Intrathecal ^{131}I-labeled antitenascin monoclonal antibody 81C6 treatment of patients with leptomeningeal neoplasms or primary brain tumor resection cavities with subarachnoid communication: phase I trial results. *Clin Cancer Res* 1996;2:963–972.
8. Sorenson JA, Phelps ME. *Physics in nuclear medicine*. Orlando, FL: Grune and Stratton; 1987.
9. Weber DA, Ivanovic M, Franceschi D, et al. Pinhole SPECT: an approach to in vivo high resolution SPECT imaging in small laboratory animals. *J Nucl Med* 1994;35: 342–348.
10. Jaszczak RJ, Li J, Wang H, Zalutsky MR, Coleman RE. Pinhole collimation for ultra-high-resolution, small-field-of-view SPECT. *Phys Med Biol* 1994;39:425–437.
11. Johnson EL, Jaszczak RJ, Wang H, Li J, Greer KL, Coleman RE. Pinhole SPECT for imaging indium-111 in the head. *IEEE Trans Nucl Sci* 1995;42:1126–1132.
12. Gilland DR, Johnson EL, Turkington TG, Coleman RE, Jaszczak RJ. Evaluation of a pinhole collimator for I-131 SPECT head imaging. *IEEE Trans Nucl Sci* 1996;43: 2230–2238.
13. Israel O, Iosilevsky G, Front D, et al. SPECT quantitation of iodine-131 concentration in phantoms and human tumors. *J Nucl Med* 1990;31:1945–1949.
14. Green AJ, Dewhurst SE, Begent RHJ, Bagshawe KD, Riggs SJ. Accurate quantification of ^{131}I distribution by gamma camera imaging. *Eur J Nucl Med* 1990;16:361–365.
15. Specht HD, Brown PH, Hanada JM, Miley AA. Importance of collimator selection for quantitative ^{131}I scintigraphy. *Nucl Med Commun* 1991;12:645–654.
16. Pollard KR, Bice AN, Eary JF, Durack LD, Lewellen TK. A method for imaging therapeutic doses of iodine-131 with a clinical gamma camera. *J Nucl Med* 1992;33: 771–776.
17. Eary JF, Pollard KR, Durack LD, et al. Post therapy imaging in high dose I-131 radioimmunotherapy patients. *Med Phys* 1994;21:1157–1162.
18. Macey DJ, Grant EJ, Bayouth JE, et al. Improved conjugate view quantitation of I-131 by subtraction of scatter and septal penetration events with a triple-energy window method. *Med Phys* 1995;22:1637–1643.
19. Smith MF, Jaszczak RJ, Wang H. Pinhole aperture design for ^{131}I tumor imaging. *IEEE Trans Nucl Sci* 1997;44:1154–1160.
20. Li J, Jaszczak RJ, Coleman RE. Quantitative small field-of-view pinhole SPECT imaging: initial evaluation. *IEEE Trans Nucl Sci* 1995;42:1109–1113.
21. Jaszczak RJ, Greer KL, Floyd CE Jr, Harris CC, Coleman RE. Improved SPECT quantification using compensation for scattered photons. *J Nucl Med* 1984;25:893–900.
22. Li J, Jaszczak RJ, Greer KL, Coleman RE. A filtered backprojection algorithm for pinhole SPECT with a displaced centre of rotation. *Phys Med Biol* 1994;39:165–176.
23. Chang L-T. A method for attenuation correction in radionuclide computed tomography. *IEEE Trans Nucl Sci* 1978;NS-25:638–643.
24. Smith MF, Jaszczak RJ, Coleman RE. Use of an analytic model of pinhole aperture penetration for resolution recovery in I-131 pinhole SPECT [Abstract]. *J Nucl Med* 1997;38(suppl):58P–59P.
25. Smith MF, Jaszczak RJ, Wang H, Li J. Lead and tungsten pinhole inserts for I-131 SPECT tumor imaging: experimental measurements and photon transport simulations. *IEEE Trans Nucl Sci* 1997;44:74–82.
26. Kemp BJ, Prato FS, Dean GW, Nicholson RL, Reese L. Correction for attenuation in technetium-99m-HMPAO SPECT brain imaging. *J Nucl Med* 1992;33:1875–1880.
27. Turkington TG, Gilland DR, Jaszczak RJ, Greer KL, Coleman RE, Smith MF. A direct measurement of skull attenuation for quantitative SPECT. *IEEE Trans Nucl Sci* 1993;40:1158–1161.
28. Stodilka RZ, Kemp BJ, Prato FS, Nicholson RL. The limitations of uniform attenuation correction for brain SPECT quantification [Abstract]. *J Nucl Med* 1997; 38(suppl):211P–212P.
29. Rajeevan N, Innis RB, Ramsby Q, Zoghbi SS, Seibyl JP, Zubal IG. Evaluation of nonuniform attenuation correction in quantitative brain SPECT imaging [Abstract]. *J Nucl Med* 1997;38(suppl):213P–214P.